Uncertainty analysis of Altantic salmon fish scale's acoustic impedance using 30 MHz C-Scan measurements

Komal Agarwal [a,1], Shivam Ojha [b,1], Roy Ambli Dalmo [c], Tore Seternes [c], Amit Shelke [b], Frank Melandsø [a] and Anowarul Habib [a,*]

[a] Department of Physics and Technology, UiT The Arctic University of Norway, 9037 Tromsø, Norway
[b] Department of Civil Engineering, Indian Institute of Technology Guwahati, 781039 Guwahati, Assam, India
[c] Norwegian College of Fishery Science, Faculty of Biosciences, Fisheries and Economics, UiT The Arctic University of Norway, 9037, Tromsø, Norway

ARTICLE INFO

ABSTRACT

Understanding the biomechanics of fish scales is crucial for their survival and adaptation. Ultrasonic C-scan measurements offer a promising tool for non-invasive characterization, however, existing literature lacks uncertainty analysis while evaluating acoustic impedance. This article presents an innovative integration of uncertainty into the analytical framework for estimating stochastic specific acoustic impedance of salmon fish scale through ultrasonic C-scans. In this study, the various types of uncertainties arising due to variation in biological structures and aging, measurement errors, and analytical noises are combined together in the form of uncertain reflectance. This uncertain reflectance possesses a distribution which is derived using a theory of waves by assuming suitable stochasticity in wavenumber. This distribution helps in development of a stochastic-specific acoustic impedance map of the scales which demonstrates the possible deviations of impedance from mean value depending on uncertainties. Furthermore, maximal overlap discrete wavelet transform is employed for efficient time–frequency deconvolution and Kriging for spatial data interpolation to enhance the robustness of the impedance map, especially in scenarios with limited data. The framework is validated by accurately estimating the specific acoustic impedance of well-known materials like a pair of target medium (polyvinylidene fluoride) and reference medium (polyimide), achieving over 90% accuracy. Moreover, the accuracy of the framework is found superior when compared with an established approach in the literature. Applying the framework to salmon fish scales, we obtain an average specific acoustic impedance of 3.1 MRayl along with a stochastic map visualizing the potential variations arising from uncertainties. Overall, this work paves the way for more accurate and robust studies in fish scale biomechanics by incorporating a comprehensive uncertainty analysis framework.

1. Introduction

Scanning acoustic microscopes are widely used in materials science and biology for non-destructive and non-invasive imaging of surface and internal structures [1,2]. It enables the inspection of materials and can provide quantitative information like the thickness of the sample, the velocity of sound in the sample, subsurface defects, and Young's modulus [3,4]. This versatile technology is widely used for mechanical characterization, including surface and subsurface evaluations, structural health monitoring (SHM) of composite structures, defects in polymer circuits, and analysis of anisotropic phonon propagation [5–7]. Many studies have scrutinized the acoustic characteristics of various biological tissues and biological-like tissues, with an increasing focus on evaluating frequencies surpassing 25 MHz [8–13]. This heightened

attention is attributed to the rising significance of high-frequency ultrasound in life science applications. The non-destructive, non-invasive, and deep penetrating imaging capabilities of these microscopes unlock the potential of acoustic imaging in biomimetics. This technology offers comprehensive evaluations of both biological samples and bio-mimicked synthetic materials, providing invaluable insights for the advancement of material development [14–17].

The age structure of a fish population provides vital insights into population dynamics crucial for fisheries and conservation management [18,19]. For many species, hard structures like scales serve as indicators of age. Atlantic salmon, inhabiting temperate and subarctic regions of the North Atlantic [20], offer ecosystem services and are economically valuable [21] but face challenges due to their complex

---

life history and habitat diversity. Most salmon populations are anadromous, spending one to six years in rivers [22] before migrating to the ocean for feeding [23,24] and returning to freshwater to spawn after one to eight years at sea [25]. Various factors, including habitat degradation and over-exploitation [24], impact salmon populations across their life cycle. The ecological and economic significance of Atlantic salmon heightens the importance of implementing efficient methods for monitoring wild salmon stocks [18]. For over a century, salmon scales have been indispensable for estimating age and growth, with their patterns reflecting river and sea age, spawning history, and origin. These scales exhibit differences in stiffness due to variations in life history, which can be non-destructively assessed using acoustic imaging to estimate specific acoustic impedance values. It is worth noting that the mechanical properties, such as stiffness, of fish scales also serve as indicators of fish health and can aid in disease diagnosis and the extraction of biological information. Additionally, beyond estimating fish age and health, the acoustic properties can indicate the mechanical properties of the fish scale. These properties not only inspire fish scale-based biomimetic studies [26,27] but also provide valuable insights into the design of biomimetic materials with applications in protective armor. The traditional optical observation methods encounter challenges such as limited depth of penetration and difficulties in imaging live samples [28]. Additionally, the use of lasers in conventional methods poses a potential risk of damaging sensitive biological samples [29]. Exploiting the advanced capabilities of scanning acoustic microscopy in carrying out C-scan imaging, it emerges as a particularly suitable approach for obtaining detailed images of fish scales. This not only enhances our comprehension of fish ecology but also contributes to advancements in fish biology and biomimetics. Thus, ultrasonic C-scan imaging has overcome the limitations of traditional observation methods and positions it as a valuable tool for studying biological structures with precision and depth.

The multifaceted potential of salmon scales in bio-inspired armor and disease diagnosis underscores their paramount importance. Moreover, their wide variety and climatic exposure will introduce certain variations in the specific acoustic impedance. Currently, the impact of these uncertainties on the estimation of specific acoustic impedance remains largely unexplored, and limited research exists that address uncertainty in ultrasonic imaging. For instance, Song and Yang utilized Bayesian deep learning to quantify uncertainty in guided wave imaging [30]. Similarly, in biology and medical research, Dohopolski et al. uses CNN with uncertainty to predict lymph node metastasis in cancer patients [31]. Further, Laves et al. presents the work related to the re-calibration of uncertainties, especially for medical imaging [32]. These studies address uncertainty using surrogate models, yet translating these into analytical forms remains challenging. Additionally, inherent uncertainties arise from biological variability, measurement errors, and analytical limitations in signal processing. The current study has consolidated various uncertainties, considering them to manifest as uncertain reflectance. The distribution of the reflection coefficient is deduced by presuming randomness in the wavenumber, leveraging the central limit theorem. Consequently, this study introduces an analytical approach for the stochastic formulation of reflectance as well as specific acoustic impedance.

Recently, Hiremath et al. presented reviews of the methods for measuring specific acoustic impedance techniques [33]. The indirect methods presented in the literature are based on the phase difference technique or resonance method to estimate the characteristic frequency. However, a two-dimensional specific acoustic impedance imaging method was introduced for characterizing biological tissues with micro-scale resolution [34,35]. This approach has been subsequently enhanced, leading to the development of three-dimensional mapping. The acoustic response obtained after scanning acoustic microscopy has a variety of frequency bands that arise due to the multiple reflection interfaces and these frequencies are evolving with time which

ultimately creates the need for time–frequency analysis of decomposition. The basic methods for observing such signals are short-term Fourier transform (STFT) [36] and analysis of such signals are time windowing and Fourier transform, which breaks signals into temporal and frequency components. Time windowing is difficult as it requires precision in the time selection as well and multiple signal bands can overlap within the time window causing issues in decomposition. Moreover, the Fourier analysis involves pre-processing steps like data windowing. Recently, Prastika et al. implemented the least square-based deconvolution methods for the time and frequency analysis of signals [37]. Advanced tools like wavelet transform use wavelet deconvolution which has better signal decomposition in the multi-scale resolution [38]. It possesses several advantages over conventional approaches like lengthening of wavelength, and cosine-tapered windowing. Wavelet transforms offer excellent time resolution allowing for precise localization of features in both time and frequency. It is well-suited for analyzing non-stationary signals because they can adapt their window size to capture both high and low-frequency components effectively. Further, when focusing on specific frequency components within the signal, a longer wavelength might encompass a broader range of frequencies, making it harder to isolate the features of interest. Wavelet transforms allow for targeted analysis by decomposing the signal into components localized in both time and frequency, enabling the extraction of specific features based on their frequency content. Among wavelet decomposition, discrete wavelet transform (DWT) imposes restrictions on the length of signals, which should be the multiple of powers of two. This limitation restricts the DWT application, and decomposition depends on whether the event span falls within a wavelet averaging window or not [39,40]. Thus, this work utilizes the maximal overlap discrete wavelet transform (MODWT) which persists down-sampled values at each decomposition level [38,40]. Thus, attributing the advantages of the MODWT, its combination with other methods will create an effective and efficient approach for extracting the characteristic features through the acoustic response of fish scales.

The article presents the integration of uncertainty in the analytical framework of estimating specific acoustic impedance. This stochastic formulation helps in estimating the possible deviation of impedance from the mean values due to various uncertainties combined together in the form of uncertain reflectance. Further, an automatic deconvolution methodology is adopted for extracting dominant frequencies from the acoustic signal through MODWT combined with a bandpass filter, thus building up a basis for the estimation of specific acoustic impedance. Lastly, Kriging is employed for spatial interpolation of specific acoustic impedance which uses both linear and Gaussian variograms. The Gaussian-based Kriging is also referred to as Gaussian process regression (GPR). It is flexible and can handle complexities in non-linear mapping [41]. This especially helps in the absence or limitation of proper spatial datasets. The proposed algorithm is validated on known materials before application to bio-samples. Fig. 1 depicts the overall strategy used in this article. Overall, our approach aims to deepen our understanding of fish biomechanics, considering real-time variations along with measurement and analytical errors, and offer improved insights into the broader marine ecosystem and revolutionizing the diagnosis of diseases and structural changes within marine communities.

2. Research contribution and significance of the study

This research presents a significant breakthrough in acoustic impedance estimation for biological materials, especially fish scales. The core innovation lies in explicitly modeling uncertainties arising from biological variations, measurement errors, and analytical limitations. These uncertainties are incorporated by representing them as variations in the reflectance coefficient, modeled using a normal distribution derived through the central limit theorem and assumptions of randomness in the wavenumber. Furthermore, the proposed
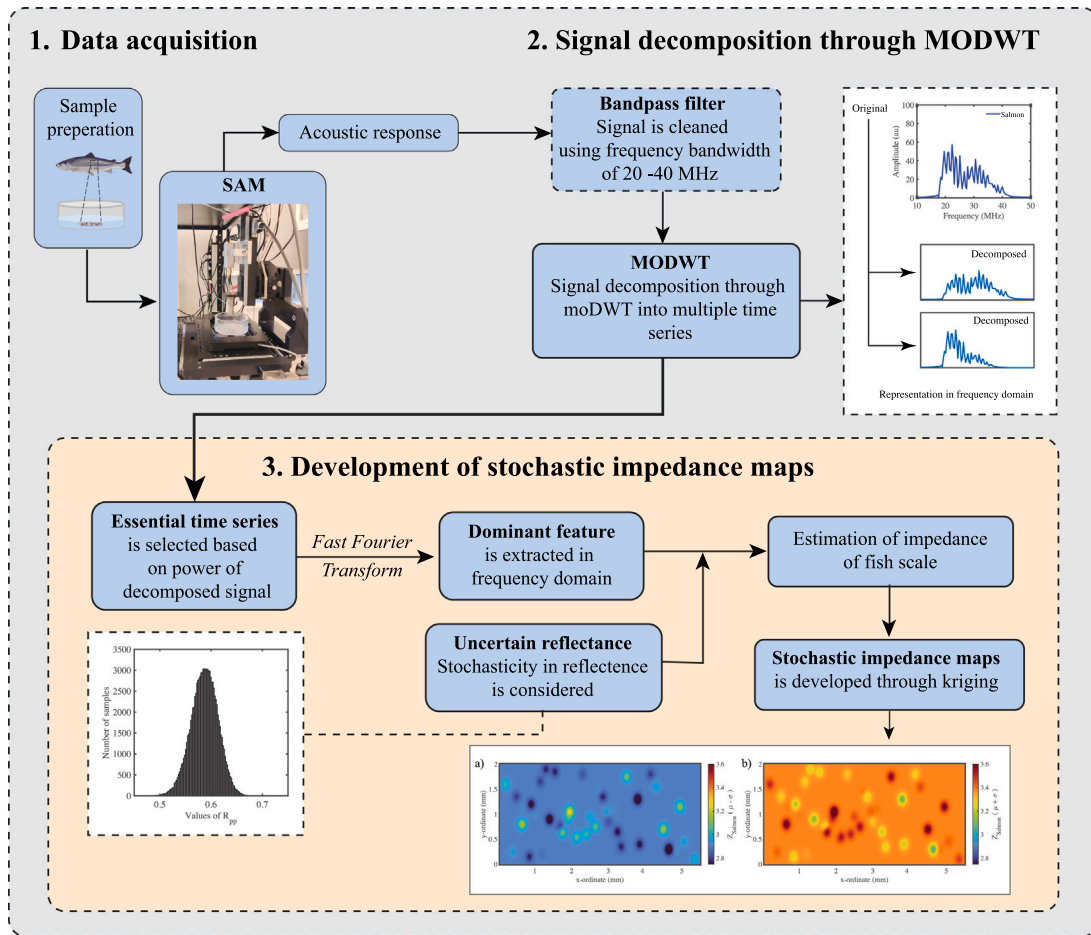
Fig. 1. The schematic diagram depicts the entire process for creating the stochastic specific acoustic impedance map of the fish scale. The initial step involves SAM imaging, which records the images of multiple samples. In the second section, we decompose the acoustic response, and then we proceed with the decomposed time series. The final section illustrates the selection of essential time series and the development of stochastic-specific acoustic impedance maps using uncertain reflectance.

framework incorporates a superior method for extracting characteristic frequencies, optimized for biological samples. This enhanced approach enables flexible, accurate, and automated feature extraction, minimizing the need for manual interventions. The methodology is robustly validated using a known polymer material (PVDF) and subsequently applied to the estimation of specific acoustic impedance in fish scales. Thus, the incorporation of uncertainty modeling in the domain leads to more realistic and reliable material assessments. This research holds significant value for various fields:

1. **Fisheries and conservation:** The potential for non-destructive age estimation and health monitoring using acoustic techniques offers a powerful tool for sustainable resource management in the fishing industry. Within fish biology, the normal age quantification is done by examining scale or otolith samples, using microscopes. Both samples involve destructive processes. The former is done by picking scales from the fish which creates tiny wounds on the skin that become an easy entrance port for pathogens. While extraction of the otolith involves the killing of fish. The development of non-destructive acoustic age estimation methods enables real sustainable resource management practices. By providing accurate fish age data, it aids in monitoring population dynamics, establishing responsible catch limits, and evaluating conservation efforts. Additionally, analyzing variations in acoustic impedance could offer crucial insights into fish health, facilitating the early detection of disease outbreaks and promoting proactive health management.

2. **Ultrasonics:** The introduction of uncertainty modeling enhances the reliability and accuracy of ultrasonic measurements across a wide range of applications in both applied and fundamental ultrasonics. The techniques developed here can be adapted to other biological tissues and biomimetic materials.

3. **Medical imaging:** The advancements in uncertainty modeling inspire improvements in medical imaging, leading to more reliable diagnoses and personalized treatments.

4. **Biomimetics:** The insights gained from the acoustic properties of fish scales can inform the development of new materials with tailored properties for diverse applications like protective armor and underwater acoustics.

3. Experimental procedure

3.1. Sample preparation

Salmon fish scales were obtained from healthy salmon obtained from the Tromsø Aquaculture Station. No ethical approval had to be obtained since the fish received no treatment before euthanization. The fish scales were carefully pulled from the fish skin, by gentle pulling with a plastic tweezer. This approach was adopted to ensure that the fish scale samples remained intact and undamaged during the extraction process.

A solution was prepared by dissolving 2 wt% of agarose (specifically, ultra-low gelling temperature agarose from Sigma Aldrich) in 10 ml of distilled water. To ensure proper mixing, we used a magnetic stirrer to agitate the mixture in a beaker, maintaining a temperature
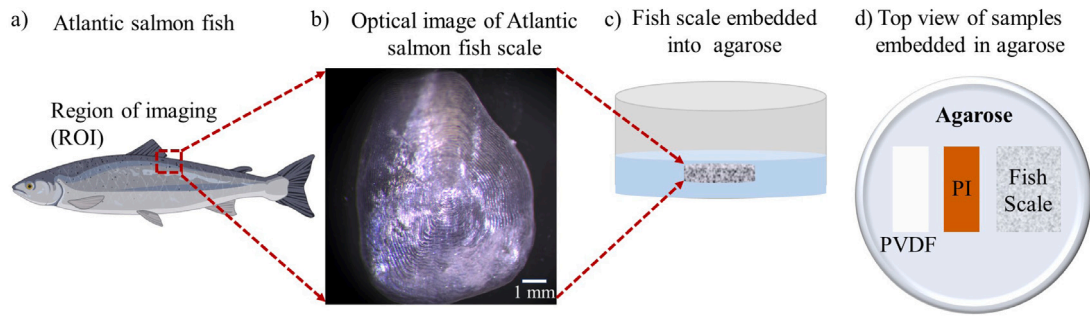
Fig. 2. A schematic representation of steps involved in sample preparation. (a) shows the sampling ROI located near the dorsal fin of the Atlantic salmon used for SAM imaging, (b) shows an optical image of a fish scale taken from the ROI, (c) shows how an extracted fish scale is embedded into the agarose gel (blue), water is filled on top (gray) for coupling in SAM imaging, (d) shows the top view to illustrate the spatial arrangement of the reference samples PVDF and polyimide (PI) with respect to the target sample fish scale.

of 100 °C for 10 min. Afterward, we poured a thick gel into a Petri dish, and on top of this gel, we carefully placed a fish scale and gently pressed it into the agarose layer (Fig. 2c). A schematic illustration of the sample preparation process is depicted in the following Fig. 2. We gently poured cold distilled water into the Petri dish and promptly began the data collection process to preserve the sample's integrity. The utilization of agarose was twofold in its purpose. Firstly, it was employed to preserve the freshness of the sample, ensuring that it remained in an optimal condition for imaging. Secondly, agarose acted as a reliable means to anchor the scale securely within the water bath, preventing any unwanted movement or displacement during the scanning process [42]. Additionally, agarose possesses a specific acoustic impedance that closely matches with water [43].

To determine the specific acoustic impedance of the fish scale, two additional samples with known specific acoustic impedances, polyimide (PI) and polyvinylidene fluoride (PVDF), were also incorporated into the agarose gel, as illustrated in Fig. 2d. This method enabled the acquisition of images for all the samples in a single session, simplifying the comparative analysis.

3.2. Scanning acoustic microscopic imaging

Fig. 3 demonstrates a labeled representation of a SAM, utilized for capturing images of samples. SAM utilizes both reflection and transmission modes, each providing distinct insights into different aspects of the sample's characteristics. The annotated image of SAM in Fig. 3 highlights its key components or operational settings, serving as a reference for image acquisition. Further details regarding the operational principles for these modes can be found in the following literature [44,45].

In this article, we primarily focus on using the reflection mode for scanning samples. To accomplish this, a frequently used method involves employing a concave spherical sapphire lens rod to concentrate acoustic energy through a coupling medium, often water. Ultrasonic signals, which are excited by a signal generator, are directed toward the sample. When these signals bounce back from the surface of the sample, the reflected waves are captured and converted into a digital signal, typically known as an A-scan or amplitude scan. To generate a C-scan image of the sample, this process is performed at several different positions within the XY plane. Another perspective on visualizing a C-scan is to regard it as the integration of A-scans in two dimensions. We developed a custom-designed ultrasound scanning system by combining a Leica DMi8 inverted microscope with a high-precision ASI MS-2000 XYZ scanning stage [46]. LabVIEW software was utilized to control both the scanning stage and other microscope components. The ultrasound functionality was realized through the integration of PXIe FPGA modules and FlexRIO hardware from National Instruments, which were installed in a PXIe chassis (PXIe-1082). The hardware consisted of an arbitrary waveform generator (AT-1212) and a 3 W RF-amplifier [47]

for ultrasound pulse generation. Additionally, a 12-bit high-speed (1.6 Gs/s) digitizer (NI-5772) was used for reflected signal recording.

We used a 30 MHz PVDF-focused Olympus transducer with specific dimensions - a 6.35 mm aperture and around 12.5 mm focal length [47]. To ensure accuracy, the thickness of the PVDF, PI film, and fish scale was measured using a digital micrometer, with approximate thicknesses of 105 μm, 130 μm, and 100 μm, respectively. We scanned the samples within a scanning area of 10 mm × 2 mm, and each pixel represented a size of 50 μm in both the x and y dimensions. We performed scans that covered a range from 200 μm above to 800 μm below the focal point of the thickest sample (PI), using a step size of 20 μm. This meticulous approach was taken to guarantee that all samples, regardless of their varying thicknesses, were imaged at their focal planes. Additionally, it allowed us to obtain z-scans of the samples at various depths, ensuring comprehensive data acquisition. Additionally, to view the entire features of a fish scale, we imaged a full/complete area of a fish scale using SAM. Fig. 4 shows the acoustic amplitude image of the full fish scale captured at the focal point plane, with a scanning area of 13 mm × 13 mm, and with x and y pixel size of 50 μm. The circular ridges that are present on top of a fish scale (as also seen in the optical image of Fig. 2d) can be seen clearly in this amplitude image. It is important to note here that the discrepancy may arise between the optical and acoustic images due to the different conditions under which they are captured. The optical image is obtained by removing the sample from the water, potentially leading to dehydration and subsequent alterations in the sample's acoustical properties. Further, a lesser area is scanned in SAM due to its own limitations. Consequently, a mismatch occurs between the optical and acoustic images. However, it is noteworthy that the scales imaged optically and acoustically originate from the same area, ensuring consistency in the data acquisition process.

4. Theory of acoustic waves

Acoustic microscopy functions in a non-destructive manner, employing the penetration of acoustic waves to render internal features visible. This propagation of acoustic waves induces both normal and shear stress within the medium, playing a crucial role in categorizing the waves into P waves (Primary or Pressure waves) and S waves (Secondary or Shear waves). In the context of a planar interface, the incidence of the P-wave results in four distinct wave components: (a) reflected P wave (RPP), (b) reflected S wave (RPS), (c) transmitted P wave (TPP), and (d) transmitted S wave (TPS). To express these wave phenomena mathematically, the wave potentials can be articulated as follows [48]:

$$\phi_{IP} = e^{ikx_1 - i\eta_1 x_2} \tag{1}$$

$$\phi_{RPP} = R_{PP}e^{ikx_1 + i\eta_1 x_2}, \quad \phi_{TPP} = T_{PP}e^{ikx_1 - i\eta_2 x_2} \tag{2}$$

$$\psi_{RPS} = R_{PS}e^{ikx_1 + i\beta_1 x_1}, \quad \psi_{TPS} = T_{PS}e^{ikx_1 - i\beta_2 x_2} \tag{3}$$
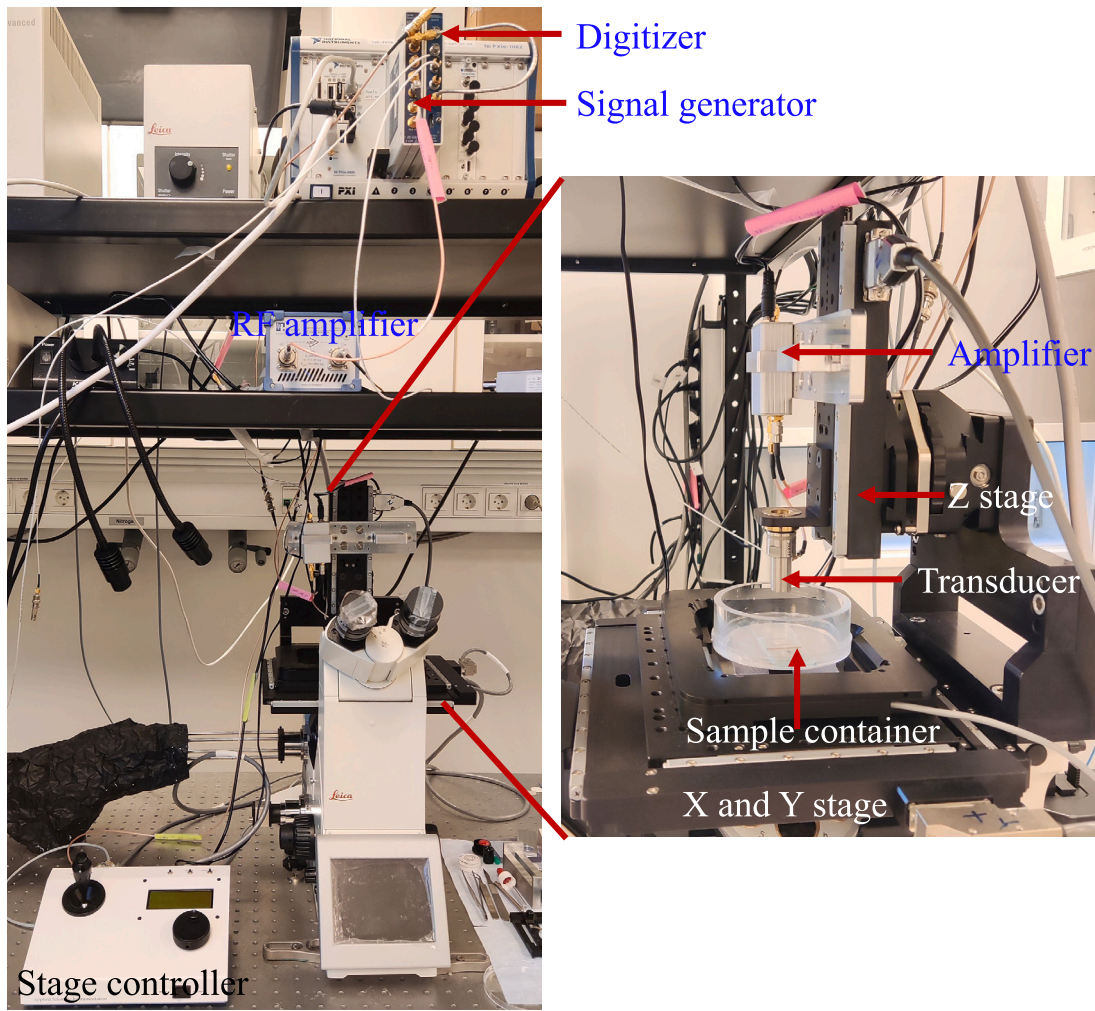
Fig. 3. The figure shows a labeled image of the SAM that was used for image acquisition of samples in this article. The experimental setup displayed in the figure demonstrates all the essential components of the SAM.
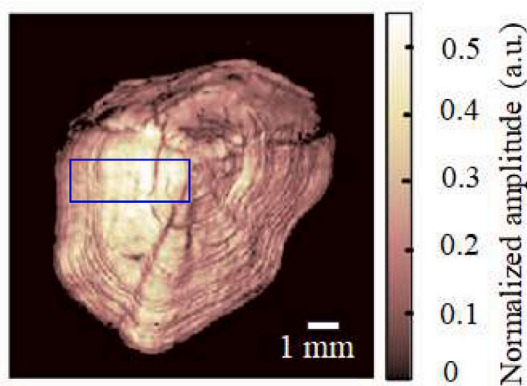

Fig. 4. Representation of the SAM image of the salmon scale. Imaging was performed employing a 30 MHz focused polymer transducer. The scanning area was 13 mm × 13 mm and the step size was 50 μm in both directions. The specific acoustic impedance was determined by considering the highlighted blue-marked rectangle area in the analysis.

where subscript numbers 1 and 2 represent the medium and,

$$k = k_{P1} sin\theta_{P1} = k_{S1} sin\theta_{S1} = k_{P2} sin\theta_{P2} = k_{S2} sin\theta_{S2} \qquad (4)$$

$$\eta_1 = k_{P1} \cos\theta_{P1}, \eta_2 = k_{P2} \cos\theta_{P2} \qquad (5)$$

$$\beta_1 = k_{s1} \cos\theta_{s1}, \beta_2 = k_{s2} \cos\theta_{s2} \qquad (6)$$

$$k_{P1} = \frac{\omega}{c_{P1}}, k_{P2} = \frac{\omega}{c_{P2}}, k_{S1} = \frac{\omega}{c_{S1}}, k_{S2} = \frac{\omega}{c_{S2}} \qquad (7)$$

where $k_{P1}, k_{P2}, k_{S1}, k_{S2}$ represent the wavenumber of P and S waves traveling in materials 1 and 2, respectively, and other symbols carry their standard meanings. In the specific scenario of normal incidence of the P-wave, i.e., $\theta_{P1} = 0, \theta_{P2} = 0, \theta_{S1} = 0, \theta_{S2} = 0$, the continuity of displacements and stress conditions at the interface yields the following simplified matrix:

$$\begin{bmatrix} k_{P1} & k_{P2} \\ -k_{S1}^2 & k_{S2}^2 \mu_{21} \end{bmatrix} \begin{Bmatrix} R_{PP} \\ T_{PP} \end{Bmatrix} = \begin{Bmatrix} k_{P1} \\ k_{S1}^2 \end{Bmatrix} \qquad (8)$$

Here, $\lambda_{21} = \lambda_2/\lambda_1$ represents the ratio of lame's constants, and the values of reflectance R_{PP} are determined as follows:

$$R_{PP} = \frac{k_{P1}k_{S2}^2\lambda_{21} - k_{P2}k_{S1}^2}{k_{P1}k_{S2}^2\lambda_{21} + k_{P2}k_{S1}^2} = \frac{Z_2 - Z_1}{Z_2 + Z_1} \qquad (9)$$

where, Z_1 and Z_2 denote the specific acoustic impedance of the medium 1 and 2, respectively.

4.1. Stochastic formulation of reflectance

In the current work, it is assumed that the wavenumber is not deterministic; rather, it follows the normal distribution with some mean and standard deviation This assumption is purely based on the

fundamentals of the center limit theorem. An uncertain wavenumber or momentum uncertainty implies a spread or uncertainty in the wave function's spatial properties. It suggests that the wave particle's position is not precisely defined but rather distributed over a range of positions. This assumption serves as a way to model the collective effect of biological uncertainties, measurement errors, and analytical uncertainties relevant to our current research.

Let us consider the wavenumber to be normal distributed, this implies $k_{P1} \sim N\left(\mu_{P1}, \sigma_{P1}\right)$, $k_{S1} \sim N\left(\mu_{S1}, \sigma_{S1}\right)$, and $k_{P2} \sim N\left(\mu_{P2}, \sigma_{P2}\right)$, $k_{S2} \sim N\left(\mu_{S2}, \sigma_{S2}\right)$, then mean and variance of the reflectance will be derived using logarithmic transformation. Taking log on both sides of Eq. (9), the resulting expression would be:

$$\ln R_{PP} = \ln\left(k_{P1}k_{S2}^2\mu_{21} - k_{P1}k_{S1}^2\right) - \ln\left(k_{P1}k_{S2}^2\mu_{21} + k_{P2}k_{S1}^2\right) \tag{10}$$

By expanding the right side of the equation using Taylor series expansion of $\ln(x)$ up to second order approximation as $\ln x = (x-1) - \frac{(x-1)^2}{2}$, we obtain:

$$\ln R_{PP} = \left\{\left(k_{P1}k_{S2}^2\mu_{21} - k_{P2}k_{S1}^2 - 1\right) - 0.5*\left(k_{P1}k_{S2}^2\mu_{21} - k_{P2}k_{S1}^2 - 1\right)^2\right\}$$
$$- \left\{\left(k_{P1}k_{S2}^2\mu_{21} + k_{P2}k_{S1}^2 - 1\right) - 0.5*\left(k_{P1}k_{S2}^2\mu_{21} + k_{P2}k_{S1}^2 - 1\right)^2\right\} \tag{11}$$

$$\ln R_{PP} = -4k_{P2}k_{S1}^2 + 2k_{P1}k_{S2}^2\mu_{21}k_{P2}k_{S1}^2 \tag{12}$$

Thus, we have obtained an approximation of $\ln R_{PP}$. Moreover, it is important to note that the accuracy of the approximation increases if fourth-order logarithmic expansion is considered instead of second-order expansion. The derivation for the mean and variance are discussed in subsequent subsections.

Mean of $\ln \mathbf{R_{PP}}$

Through operating expectation on both sides of Eq. (12), and assuming all the wavenumbers to be independent, the mean of the $\ln R_{pp}$ is written as:

$$E\left(\ln R_{PP}\right) = -4E(k_{P2})E(k_{S1}^2) + 2\mu_{21}E(k_{P1}k_{S1}^2)E(k_{P2}k_{S2}^2) \tag{13}$$

$$E\left(\ln R_{PP}\right) = -4E(k_{P2})E(k_{S1}^2) + 2\mu_{21}E(k_{P1})E(k_{S1}^2)E(k_{P2})E(k_{S2}^2)$$
$$= -4\mu_{P2}E(k_{S1}^2) + 2\mu_{21}\mu_{P1}\mu_{P2}E(k_{S1}^2)E(k_{S2}^2) \tag{14}$$

For the evaluation of higher moments i.e., $E(X^2), E(X^4)$, we have used the properties of the moment generating function. Thus, if X follows the normal distribution, then, its moment generating function is written as $M = e^{t\mu + \frac{1}{2}\sigma^2 t^2}$, Therefore, the moments can be written as

$$E(X) = \left.\frac{dM}{dx}\right|_{t=0}, E(X^2) = \left.\frac{d^2M}{dx^2}\right|_{t=0}, E(X^3) = \left.\frac{d^3M}{dx^3}\right|_{t=0},$$
$$E(X^4) = \left.\frac{d^4M}{dx^4}\right|_{t=0} \tag{15}$$

Solving the above equation, we can write:

$$E(X^2) = \mu_X^2 + \sigma_X^2, \quad E(X^4) = \mu_X^4 + 6\mu_X^2\sigma_X^2 + 3\sigma_X^4 \tag{16}$$

Hence, the mean can be written as follows:

$$E\left(\ln R_{PP}\right) = -4\mu_{P2}\left(\mu_{S1}^2 + \sigma_{S1}^2\right) + 2\mu_{21}\mu_{P1}\mu_{P2}\left(\mu_{S1}^2 + \sigma_{S1}^2\right)\left(\mu_{S2}^2 + \sigma_{S2}^2\right) \tag{17}$$

Variance of $\ln \mathbf{R_{PP}}$

Through operating variance on both sides of Eq. (12), and assuming all the wavenumbers to be independent, the mean of the $\ln R_{pp}$ is written as:

$$Var\left(\ln R_{PP}\right) = E\left([\ln R_{PP}]^2\right) - \underbrace{\left[E(\ln R_{PP})\right]^2}_{Already\ known} \tag{18}$$

$$E\left[\left(\ln R_{PP}\right)^2\right] = E\left[16k_{P2}^2 k_{S1}^4 + 4k_{P1}^2 k_{S2}^4 \mu_{21}^2 k_{P2}^2 k_{S1}^4\right.$$
$$\left. - 16k_{P1}k_{P2}^2\mu_{21}k_{S1}^4 k_{S2}^2\right]$$
$$= 16E(k_{P2}^2)E(k_{S1}^4) + 4\mu_{21}^2 E(k_{P1}^2)E(k_{S2}^4)E(k_{P2}^2)E(k_{S1}^4)$$
$$- 16\mu_{21}\mu_{P1}E(k_{P2}^2)E(k_{S1}^4)E(k_{S2}^2) \tag{19}$$

where 2th and 4th moments are calculated using the moment regenerating function as follows:

$$E(k_{P1}^2) = \mu_{P1}^2 + \sigma_{P1}^2, \quad E(k_{P2}^2) = \mu_{P2}^2 + \sigma_{P2}^2, \quad E(k_{S2}^2) = \mu_{S2}^2 + \sigma_{S2}^2 \tag{20}$$

$$E(k_{S1}^4) = \mu_{S1}^4 + 6\mu_{S1}^2\sigma_{S1}^2 + 3\sigma_{S1}^4, \quad E(k_{S2}^4) = \mu_{S2}^4 + 6\mu_{S2}^2\sigma_{S2}^2 + 3\sigma_{S2}^4 \tag{21}$$

Evaluating mean and variance of $\mathbf{R_{PP}}$

Let mean of the R_{PP} be μ_R, then using Jensen's inequality, the approximate values of $E(R_{PP})$ is given by:

$$\ln E(R_{PP}) \approx E(\ln R_{PP}) \tag{22}$$

$$E(R_{PP}) \approx \exp(E[\ln R_{PP}]) \tag{23}$$

$$\mu_R \approx e^{E[\ln R_{PP}]} \tag{24}$$

Similarly, the variance of the R_{PP} is approximated by using delta method:

$$Var(\ln R_{PP}) \approx \frac{Var(R_{PP})}{[E(R_{PP})]^2} \tag{25}$$

$$Var(R_{PP}) \approx Var(\ln R_{PP}) \times [E(R_{PP})]^2 \tag{26}$$

Estimation of specific acoustic impedance

Considering the characterization frequency of the transmitted/incident signal, the reflected signal through reference and target medium be S_0, S_{ref} and S_{target} respectively. Then, we can write the following relations [34,48,49]:

$$S_{\text{target}} = \frac{Z_{\text{target}} - Z_{\text{sub}}}{Z_{\text{target}} + Z_{\text{sub}}}S_0, \quad S_{ref} = \frac{Z_{ref} - Z_{sub}}{Z_{ref} + Z_{sub}}S_0 \tag{27}$$

where Z_{target}, Z_{ref}, and Z_{sub} represent the specific acoustic impedance of the target, reference, and substrate, respectively. The measurement is possible only for the S_{ref} and S_{target} and S_0 cannot be measured directly. Let $S_r = \frac{S_{target}}{S_{ref}}$, and $R_{ref} = \frac{Z_{ref} - Z_{sub}}{Z_{ref} + Z_{sub}}$ The specific acoustic impedance of the target medium is subsequently is given by [50]:

$$Z_{target} = \frac{1 + S_r \cdot R_{ref}}{1 - S_r \cdot R_{ref}}Z_{sub} \tag{28}$$

Considering the uncertainty in the R_{ref} with mean μ_R and standard deviation σ_R. For the calculation of μ_R and σ_R, appropriate wavenumbers are selected with proper mean and variance. Now, The values of estimated mean μ_Z and bounds $\mu_Z \pm \sigma_Z$ for the target specific acoustic impedance are given by:

$$\mu_Z \approx \frac{1 + S_r \cdot \mu_R}{1 - S_r \cdot \mu_R}Z_{sub} \tag{29}$$

$$\mu_Z \pm \sigma_Z \approx \frac{1 + S_r \cdot (\mu_R \pm \sigma_R)}{1 - S_r \cdot (\mu_R \pm \sigma_R)}Z_{sub} \tag{30}$$

Thus, the current work considers uncertainty in the analytical framework for estimating the specific acoustic impedance of the target medium.

5. Sources of uncertainty and their considerations in framework

The sources of the uncertainties have two types (a) aleatoric and (b) epistemic which can further be sub-classified here into three types (1) biological variations, (2) measurement errors, and (3) analytic
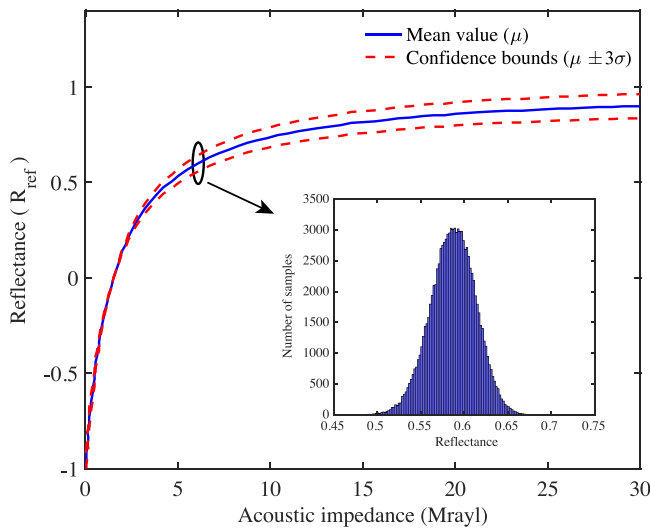
Fig. 5. Variation of reflection coefficient with the acoustic impedance considering lumped uncertainties and other variations. The location of the polyimide reflection coefficient with glass is highlighted and the variation of uncertain reflectance is presented which is derived in the analytical form by considering randomness in wavenumber as per center limit theorem. This uncertain reflectance is the result of lumped certainty and is used in the framework for the stochastic estimation of specific acoustic impedance.

uncertainties. Biological uncertainties play a significant role in introducing variability in reflection coefficient measurements. The inherent heterogeneity of biological materials, like fish scales, translates into variations in composition, structure, and density. These localized fluctuations directly affect acoustic impedance, thereby influencing how sound waves reflect off the scales. Additionally, a fish's life history and the environmental factors it experiences influence the growth patterns within its scales. These complex factors create localized differences in material properties, leading to unpredictable changes in the reflection coefficient. Furthermore, the measurement process itself introduces several potential sources of uncertainty. Surface conditions like roughness can cause scattering of the incident sound waves, leading to variations in the reflected signal and the calculated reflection coefficient. Similarly, the orientation of the scale relative to the acoustic wave significantly impacts the reflected energy. Limitations in the instrumentation, such as variations in transducer sensitivity or the presence of environmental noise, further contribute to uncertainty in the measured reflection coefficient. Even sample preparation inconsistencies, including variations in mounting, hydration, or thickness, can affect the results. Next, analytical uncertainties arise from the signal processing techniques and theoretical models employed in the analysis. For instance, the choice of algorithms and parameters used for filtering, deconvolution, and frequency analysis can introduce biases or uncertainties in the calculated reflection coefficient. Furthermore, the assumptions and simplifications embedded within theoretical models also introduce a certain level of uncertainty into the final estimations. Raum et al. has indicated that the standard deviation of reflectance can reach up to 0.033 for bone [14]. Using a similar analogy, the standard deviation of the reflectance is considered to be 0.024 for the reference medium i.e., polyimide. Thus, in this research, all the uncertainties are lumped into reflectance coefficients and it is assumed to follow a distribution derived from introducing randomness in wavenumber as per the center limit theorem. The consideration of the uncertain reflectance in the analytical framework will lead to the estimation of specific acoustic impedance in a stochastic sense. The variation of uncertainty in the reflectance is shown in Fig. 5.

6. Methodology for predicting stochastic specific acoustic impedance maps

This work proposes a methodology for developing a stochastic-specific acoustic impedance map of fish scales. The approach utilizes ultrasonic C-scan measurements in conjunction with the Maximal Overlap Discrete Wavelet Transform (MODWT) while accounting for uncertainties in the reflectance. To simplify the analysis and avoid complexities arising from multiple reflections within the fish scale, the proposed method assumes variations primarily occur in the horizontal plane, treating the vertical plane as a homogeneous medium. However, real-world scenarios with multiple interfaces beyond a single homogeneous layer can introduce challenges. These interfaces can lead to a reflected acoustic response containing multiple peaks, each with distinct frequency components. This necessitates a time–frequency analysis approach to effectively analyze such signals. Wavelet transforms excels in this situation due to its excellent time resolution. This allows for precise localization of features in both the time and frequency domains. Moreover, wavelets are well-suited for analyzing non-stationary signals like those encountered here, as they can adapt their window size to capture both high and low-frequency components effectively. In contrast, relying solely on longer wavelengths can be problematic when focusing on specific frequency components within the signal. This is because a longer wavelength encompasses a broader range of frequencies, making it difficult to isolate the features of interest. However, wavelet transforms address this challenge by decomposing the signal into components localized in both time and frequency. This targeted analysis allows for the extraction of specific features based on their unique frequency content. Before applying MODWT, the signal is first passed through a bandpass filter to remove unwanted noise, further enhancing the effectiveness of the subsequent decomposition process. MODWT then decomposes the filtered signal into multiple time series, each associated with its own wavelet and scaling coefficients for different decomposition levels.

6.1. Maximal overlap discrete wavelet transform (MODWT)

In the discrete wavelet transform (DWT), the signal is decomposed into different component levels through filtering and down-sampling, where decomposition at each level is characterized through its approximation and detailed coefficients [38–40]. Further, Mallat's algorithm is used for the practical application of DWT which contains a pair of filters: a low-pass filter (scaling function) and a high-pass filter (wavelet function). The application of Mallat's algorithm continues recursively on the resulting low-pass signal till the required decomposition level. For a discrete signal, $\mathbf{X} = \{X_t, t = 0, 1, \ldots, N-1\}$, the DWT computes the wavelet coefficient for the discrete wavelet of scale 2^j and location $2^j k$ using the following equation:

$$W_X(j, k) = 2^{-j/2} \sum_{t=0}^{N-1} X_t \psi * \left(2^{-j} t - k\right), \text{ for } s_0 = 2 \text{ and } \tau_0 = 1 \qquad (31)$$

where $W_X(j, k)$ is the wavelet coefficient and N is an integer power of two.

However, DWT is incapable of handling shift-invariance and has narrow frequency resolution, thus restricting its application to the fixed signal length with an integer multiple of a power of two [38]. A modified version called MODWT divides the frequency band of the input signal into scaling and wavelet coefficients using low- and high-pass filters, that is, scaling and wavelet filters. MODWT can be properly defined for arbitrary signal length and it achieves redundancy through an oversampled representation which enables more accurate statistical analysis [40].

Let $X = X_t, t = 0, \ldots, T-1$, be the time series data, then, the j$^{\text{th}}$ level wavelet and scaling filters are denoted as $\{\bar{h}_{jl}\}$ and $\{\tilde{g}_{jl}\}$, respectively. The scaling and wavelet coefficients calculated by Mallat's algorithm

are described as follows:

$$\tilde{W}_{j,t} = \sum_{l=0}^{T-1} \tilde{h}_{j,l} X_{t-l \bmod T}, \quad \tilde{V}_{j,t} = \sum_{l=0}^{T-1} \tilde{g}_{j,l} X_{t-l \bmod T} \tag{32}$$

where $j = 1, 2, \ldots, J_0$ is the level of wavelet decomposition, and 'mod' denotes the remainder of dividing two numbers. The wavelet $\tilde{W}_j$ and scaling $\tilde{V}_j$ coefficients vectors of MODWT are written as:

$$\tilde{W}_j = \{\tilde{W}_{j,0}, \tilde{W}_{j,1}, \ldots, W_{j,T-1}\}, j = 1, 2, \ldots, J_0 \tag{33}$$

$$\tilde{V}_j = \{\tilde{V}_{j,0}, \tilde{V}_{j,1}, \ldots, \tilde{V}_{j,T-1}\}, j = 1, 2, \ldots, J_0 \tag{34}$$

where $\tilde{V}_j$ and $\tilde{W}_j$ are related to the smallest and highest frequency components of the original signal. $\{\tilde{h}_{j,l}\}$, and $\{\tilde{g}_{j,l}\}$ are the jth level MODWT high-pass filter $(\tilde{h}_{j,l} \equiv h_{j,l}/2^{j/2})$ and low-pass filter $(\tilde{g}_{j,l} \equiv g_{j,l}/2^{j/2})$ and J_0 is the highest decomposition level. For the level 3 decomposition, the MODWT decomposes an original signal X into a low-pass filtered approximation component (A_3) and high-pass filtered detail components $(D_1, D_2$ and $D_3)$. The equations of MODWT-based multi-resolution analysis can be used for the reconstruction of decomposed signal and are written as follows:

$$\mathbf{X} = \sum_{j=1}^{L} D_j + A_{J_0}, \quad D_{j,t} = \sum_{l=0}^{n-1} \tilde{h}_{j,l} W_{j,t+l \bmod n} \tag{35}$$

Through using the above equations, the signal is reconstructed for each level of decomposition. The next challenge is to select the appropriate decomposed time series for further processing which is discussed in subsequent sections.

6.2. Selection of essential time series and estimation of specific acoustic impedance

Once, the signal is decomposed into wavelet and scaling coefficients, it is important to reconstruct the decomposed time series and select the essential time series. In order to reconstruct the decomposed time series, the necessary decomposition levels are selected. The wavelet coefficients associated with those levels were passed through inverse wavelet transform (iMODWT) to obtain the decomposed time series. Next, the power of each decomposed time series is calculated and normalized with the maximum power. Thus the time series having maximum power relative to each other is selected as the essential time series. Thus, this essential time series is then transformed into the frequency domain to extract the character's tic feature of the response. In the frequency domain, the frequency corresponding to the maximum amplitude is assumed to be the signal-characterizing feature and is used in the calculation of specific acoustic impedance.

Using the uncertain reflectance, the estimated specific acoustic impedance has its mean value as well as $\mu + \sigma$ and $\mu - \sigma$ values, thus giving rise to the stochastic prediction of specific acoustic impedance. In the current work, it is referred to as stochastic-specific acoustic impedance. The specific acoustic impedance is first calculated at sufficient points, sampled using Latin hypercube sampling, spread over the whole domain, and then kriging is performed for all the three values of stochastic specific acoustic impedance i.e., μ, $\mu+\sigma$, and $\mu-\sigma$ to find the impedance over the complete domain and stochastic specific acoustic impedance maps are generated to analyze the surface of fish scale. The basic understanding of the kriging is presented here.

Kriging [51] is a method of interpolation based on the Gaussian process. It develops a meta-model of a partially observed function (of time and/or space) with an assumption that this function is a realization of a Gaussian process (GP) [41,52], and thus the regression is also referred to as the Gaussian process regression (GPR). In GPR, the kernel functions are assumed, and the hyperparameters of the kernel functions are computed from observation via maximizing the log-marginal likelihood function. In the aspects of Kriging, the kernel function can be interpreted as a variogram, and two types of

variogram are used in the current work, i.e., linear and Gaussian. Let the known locations be represented by $X = \{x^{(i)}\}_{i=1}^{N}$ where x is the two-dimensional vector and the observed state at these locations is given by $y = \{y^{(1)}, y^{(2)}, \ldots, y^{(N)}\}$. Let the meta-model between the observed state and known locations is given by:

$$y = f(x) \sim GP(\mu(x), k(x, x')) \tag{36}$$

where $\mu(x)$ is the mean function and $k(x, x')$ is the kernel or covariance function. By definition, the prior of the observed state vector is Gaussian and is given by $p(f(x) \mid x) = \mathcal{N}(f(x) \mid \mu, K)$. Given the prediction locations as x_*, the predicted state $y_* = f(x_*)$ is also jointly Gaussian and is given by

$$\begin{pmatrix} f(x) \\ f(x_*) \end{pmatrix} \sim \mathcal{N}\left(\begin{pmatrix} \mu \\ \mu_* \end{pmatrix}, \begin{pmatrix} K & K_* \\ K_*^T & K_{**} \end{pmatrix}\right) \tag{37}$$

Using Bayesian transformation, the posterior mean and variance of the predicted state are written as

$$y(x_*) = \mu(X_*) + K_*^T K^{-1} (f(x) - \mu(x)) \tag{38}$$

$$\Sigma_* = K_{**} - K_*^T K^{-1} K_* \tag{39}$$

Lastly, the proposed methodology can be summarized as follows:

- Removal of noise through a band-pass filter
- Filtering of cleaned signal through MODWT
- Selection of essential time series
- Picking up the dominant frequency
- Estimation of mean specific acoustic impedance and its bounds
- Development of stochastic specific acoustic impedance maps

7. Results and discussion

7.1. Validation of the proposed framework

The accuracy of the proposed framework has been rigorously tested considering polyvinylidene fluoride (PVDF) as the primary material of interest, utilizing polyimide (PI) as the reference sample. The experimental process, detailed in Section 3, was meticulously described, recording the acoustic response of the system under study. In the experiment, the response has been obtained at nodes whose X and Y locations are represented by index i.e., X-index (i) and Y-index (j). However, only results from a specific node are shown for brevity. The full response signal comprises a dynamic spectrum with evolving frequencies. Thus, to separate the essential characteristics of the signal, the signal is first passed through the bandpass filter, and then decomposition is carried out using MODWT. This decomposition leads to the various time series at different decomposition levels represented by (1), (2), (3), and (4) which are shown in Fig. 6. The three peaks in the decomposed time series (refer Fig. 6) represent genuine features of the signal that are located on different frequency scales and share similarities with the main peak.

While reconstructing the decomposed time series from wavelet and scaling coefficients of necessary level as described earlier, the coefficients associated with those levels were passed through inverse wavelet transform (iMODWT), and the power of each decomposed time series is calculated and normalized. The time series that has maximum energy content is selected as the essential time series and considered as the filtered signal. Fig. 7 shows the normalized power of decomposed time series for each other.

The essential characteristics of the signal that are directly correlated to the properties of the specimen are extracted from this filtered response. However, the changes in the time domain are difficult to interpret and therefore the responses are transformed to the frequency domain where the predominant peak frequency which corresponds to the maximum amplitude is selected as a representative of the specimen characteristics as presented in Fig. 8.
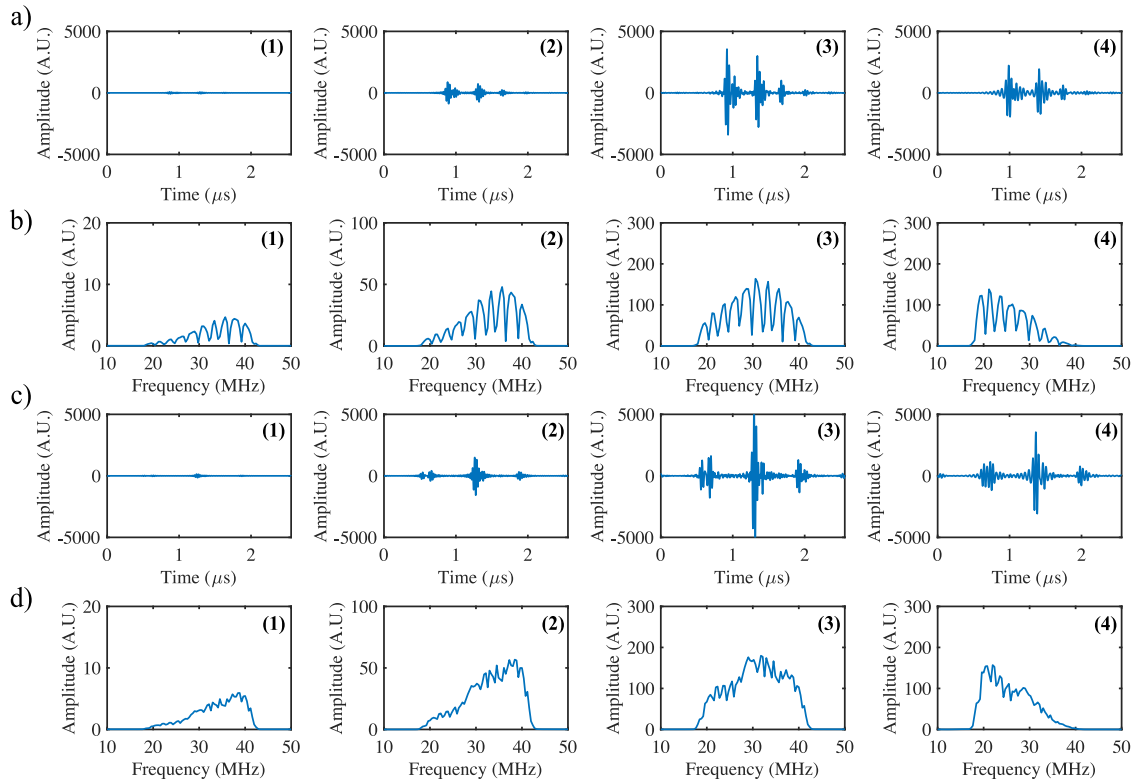
Fig. 6. It demonstrates the decomposition of the acoustic response signal into multiple decomposed time series after MODWT in both the time-domain (a), (c) as well as frequency domain (b), (d). Figures (a) and (b) highlight the characteristics of the response signal PVDF at different decomposition levels and figures (c) and (d) highlight the characteristics of the response signal of polyimide (PI) at various decomposition levels. The time series shown in (1), (2), (3), and (4) are reconstructions using specific decomposition levels of wavelet coefficients.
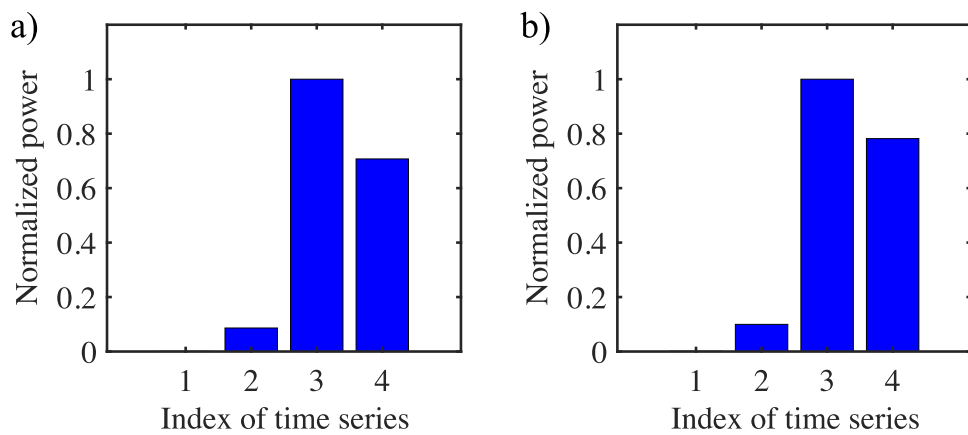

Fig. 7. The figures represent the normalized power of decomposed time series for each other for (a) PVDF and (b) polyimide (PI) samples, providing the basis for the selection of the dominant time series.
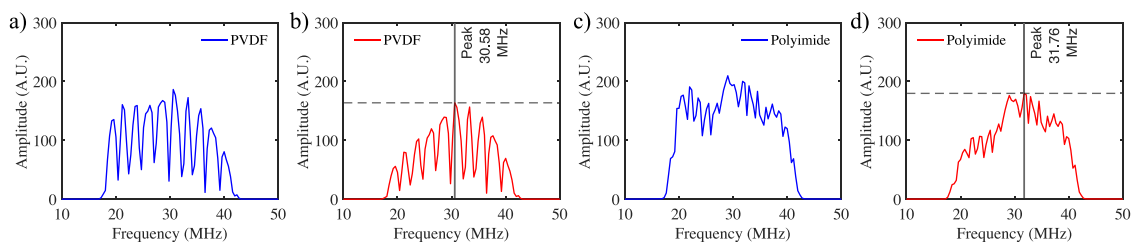

Fig. 8. Displayed in the figures are the frequency spectra of the true responses (a) and (c), as well as the wavelet-transformed signals (b) and (d). These representations provide the identification of primary frequencies.
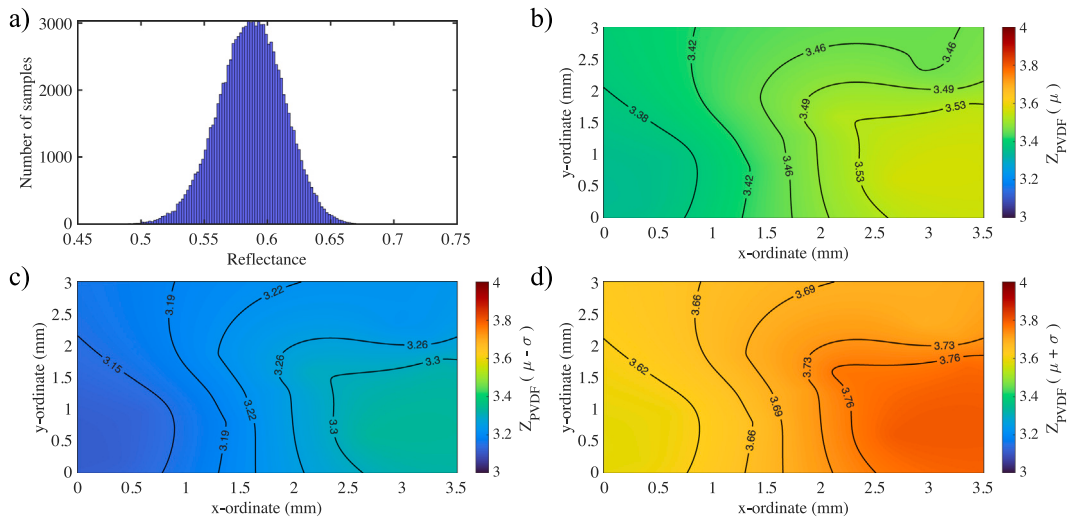
Fig. 9. (a) Illustrates the considered variation in the reflectance (b) illustrates the mean value of the specific acoustic impedance (c) and (d) demonstrates the estimated $\mu - \sigma$ and $\mu + \sigma$ of the stochastic specific acoustic impedance map due to uncertain reflectance.
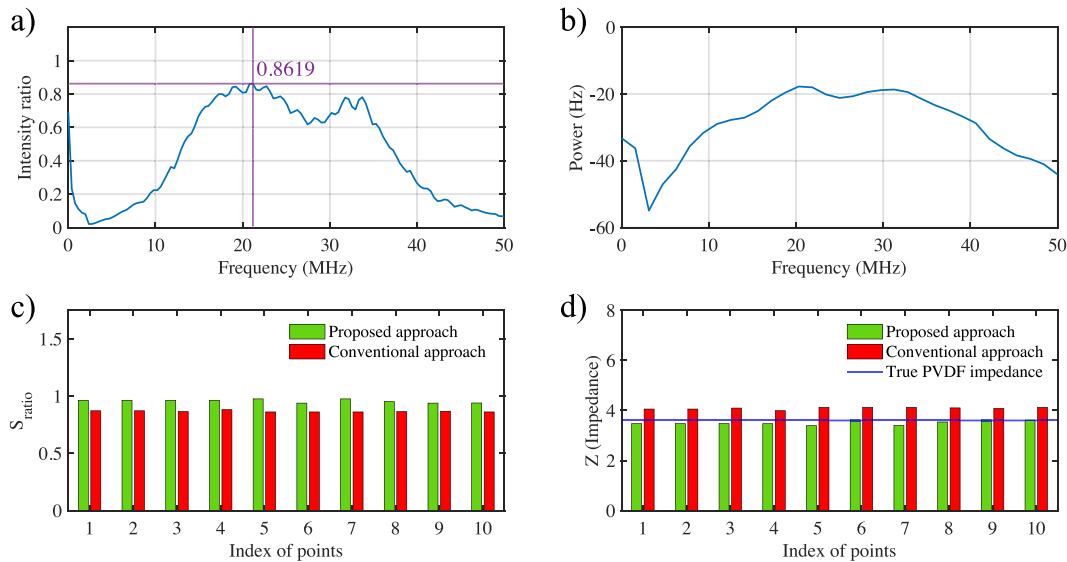

Fig. 10. (a) Normalized intensity, (b) cross power spectrum density, (c) S_{ratio} achieved through proposed and conventional approach, and (d) Estimated specific acoustic impedance (Z) from proposed and conventional approach. (a) and (b) illustrated the intensity ratio and cross power spectrum derived for the PVDF with respect to the reference medium using methodology discussed in Ref. [34].

Fig. 8(a, c) illustrates the frequency spectra of the true responses of the reference sample PVDF and target medium polyimide (PI). These obtained frequencies will provide the S_{ratio} as described in the theory section. The accuracy of the complete algorithm is determined through accurate estimation of these frequencies because the S_{ratio} is found to be very sensitive in the calculation of specific acoustic impedance. The frequency spectra of the filtered or wavelet transformed signal are shown in Fig. 8(b and d). The dominant peak from the frequency spectra of the filtered signal is obtained and shown in Fig. 8(b and d). After extraction of dominant frequencies, the stochastic specific acoustic impedance of the PVDF is calculated and thus, the estimated mean value is compared with the true specific acoustic impedance value of the PVDF along with the predicted $\mu + \sigma$ and $\mu - \sigma$. The uncertainty in the reflectance which is considered in the current work is presented in Fig. 9(a).

The estimated values of μ, $\mu + \sigma$, $\mu - \sigma$ of stochastic specific acoustic impedance map generated for the PVDF through kriging using linear variogram function is shown in Fig. 9(b), (c) and (d). Further, the proposed framework is compared with the established deterministic approach presented by [34] for estimation of mean impedance. The normalized intensity and cross-power spectrum are obtained as shown in Fig. 10. The obtained ratio in this case is 0.86 as opposed to that obtained through the proposed framework which is 0.976. Table 1 shows the calculation of 10 spatial points selected using Latin hypercube sampling where the index in the table is anonymously representing the test point's location. It can be inferred that the relative error obtained through the proposed approach is 5% in comparison to the conventional methods which is around 12%. Thus, it was verified that the proposed framework presents better results than the established framework. Moreover, it can be clearly shown that mean specific acoustic impedance values which has a very low mean absolute error of 2.88% demonstrate the efficacy and robustness of the proposed framework. Moreover, the results provided by the proposed framework is much better than the conventional approach. The next section will discuss the application of the proposed framework to the fish scale which examines its specific acoustic impedance in the present work.

Table 1
It represents the corresponding frequency, measured and true specific acoustic impedance of the target and reference specimen and also their uncertainties. Further, the results of the proposed approach are compared with the conventional approach.

X (mm)	9.9	8.25	8.7	8.55	10.25	9.7	8.85	9	10.35	9.15
Y (mm)	2.6	1.85	2	1.05	2.15	0.6	1.3	1.45	1.7	1.6
Z_{sub}	12.8	12.8	12.8	12.8	12.8	12.8	12.8	12.8	12.8	12.8
S_{PVDF}	30.980	30.588	30.588	31.373	32.157	30.196	31.373	31.373	30.196	30.980
$S_{polyimide(PI)}$	32.157	31.765	31.765	32.549	32.941	32.157	32.157	32.941	32.157	32.941
S_{ratio}	0.963	0.963	0.963	0.964	0.976	0.939	0.976	0.952	0.939	0.940
[a] S_{ratio}	0.872	0.872	0.866	0.882	0.862	0.862	0.862	0.865	0.868	0.862
μ_{Rpp}	0.595	0.595	0.595	0.595	0.595	0.595	0.595	0.595	0.595	0.595
σ_{Rpp}	0.024	0.024	0.024	0.024	0.024	0.024	0.024	0.024	0.024	0.024
Z_{true}	3.6	3.6	3.6	3.6	3.6	3.6	3.6	3.6	3.6	3.6
μ_Z	3.472	3.475	3.475	3.470	3.394	3.624	3.398	3.540	3.624	3.615
[a] Z	4.056	4.056	4.095	3.990	4.122	4.122	4.122	4.102	4.082	4.122
ε (%)	3.55	3.47	3.47	3.61	5.72	0.67	5.61	1.67	0.67	0.42
[a] ε (%)	12.65	12.65	13.76	10.82	14.49	14.49	14.49	13.94	13.39	14.49
$\mu_Z - \sigma_Z$	3.241	3.244	3.244	3.239	3.162	3.394	3.166	3.310	3.394	3.385
$\mu_Z + \sigma_Z$	3.710	3.713	3.713	3.707	3.632	3.860	3.636	3.777	3.860	3.851

[a] In the table, results from the conventional approach.

7.2. Estimation and development of the specific acoustic impedance map of fish scale

To determine the specific acoustic impedance of the fish scale, we have applied the algorithm mentioned above to analyze the acoustic response of the fish scale as marked in Fig. 4. Here also, the polyimide is used as the base material. The objective now is to isolate the dominant characteristics residing within it through MODWT. To distill the essential characteristics of the signal, it becomes necessary to apply a bandpass filter first, and then decomposition is carried out using MODWT. This decomposition leads to the various time series at different decomposition levels represented by (1), (2), (3), and (4) which are shown in Fig. 11. It shows a significant difference in the reflected frequency in both materials even in the decomposed state. Further, the three peaks in the decomposed time series represent genuine features of the signal that are located on different frequency scales and share similarities with the main peak. This variation in decomposed time series arises due to wave phenomenon, primarily due to differences in the material-specific acoustic impedance and multiple interfaces of reflection. The time series that has maximum energy content is selected as the essential time series and considered as the filtered signal. Fig. 12 shows the normalized power of each decomposed time series with respect to others. As already discussed in the previous case (PVDF and polyimide), the essential characteristics of the signal that are directly correlated to the acoustic properties of fish scales can be extracted from this filtered response forming the fundamental basis for monitoring the bio-mechanical properties through signal processing. However, the changes in the time domain are difficult to interpret and therefore the responses are transformed to the frequency domain where the predominant peak frequency is selected as a representative of the specimen characteristics as presented in Fig. 13.

Fig. 13(a and c) illustrates the frequency spectra of the true responses of the reference fish scale and target medium polyimide. These obtained frequencies will provide the S_{ratio} as described in the theory section. It serves as a foundation for specific acoustic impedance calculation, as it reveals the fundamental frequencies correlated to the material that helps us to deduce the reflectance property associated with the medium which ultimately provides the specific acoustic impedance of the fish scale through the procedure described earlier. The frequency spectra of the filtered or wavelet transformed signal are shown in Fig. 13(b and d). The dominant peak from the frequency spectra of the filtered signal is obtained and shown in Fig. 13(b and d). After extraction of dominant frequencies, the stochastic specific acoustic impedance of the fish scale is calculated and thus, the estimated mean value of the specific acoustic impedance of the fish scale along with uncertainty considered in reflectance is presented in Fig. 14(a)

and (b) respectively. The estimated values of $\mu - \sigma$, $\mu + \sigma$ of stochastic specific acoustic impedance map generated for the fish scale through kriging using Gaussian variogram is shown in Fig. 15(c) and (d).

The figures visually represent the dispersion of estimated specific acoustic impedance values, providing a holistic understanding of how impedance fluctuates throughout the entire area of interest. This representation is indispensable for gaining insights into the specific acoustic impedance characteristics of the fish scale. Figs. 14 and 15 show that the mean specific acoustic impedance values of the considered fish scale lie somewhere between 2.9 to 3.3 Mrayl. Table 2 provides the estimated impedance with corresponding bounds through proposed approach at ten random location. It can be shown that considering uncertainties in the form of stochastic reflectance, the specific acoustic impedance shows a possible deviation between 2.8 to 3.6 Mrayl. The unique composition of fish scales positions them between the pliability of soft tissues and the rigidity of bones. Our analysis yields a mean value of approximately 3.1 Mrayl for fish scales, reinforcing the robustness of our proposed framework. Further, the specific acoustic impedance map reveals localized spots with both high and low values, deviating from a uniform distribution across the entire domain. This variability may be attributed to diverse factors such as human interventions and uncertainties inherent in the measurement process. Thus, the proposed algorithm not only refines the estimate of specific acoustic impedance but also offers a more accurate depiction by considering uncertainties and showing the possible deviation of impedance from the mean value.

8. Conclusion

This work presented a novel framework for estimating the stochastic specific acoustic impedance of fish scales using ultrasonic C-scans. By incorporating uncertainty analysis through the concept of uncertain reflectance, the study addressed a critical gap and acknowledges the inherent variability arising from biological variations, measurement errors, and analytical noise while evaluating the possible deviation of the specific acoustic impedance. The framework's effectiveness is first established and verified by analyzing the specific acoustic impedance characteristics of well-known materials. In this context, PVDF is used as a reference material for calibration, ensuring the accuracy of our proposed algorithm. The results confirm that the estimated specific acoustic impedance through the proposed framework closely aligns with the actual values for PVDF, demonstrating an accuracy exceeding 90%. Additionally, the proposed approach is compared with the existing conventional approach, revealing that the error obtained through the proposed approach is within 5% compared to the 12% error obtained through the conventional approach. The derived distribution of
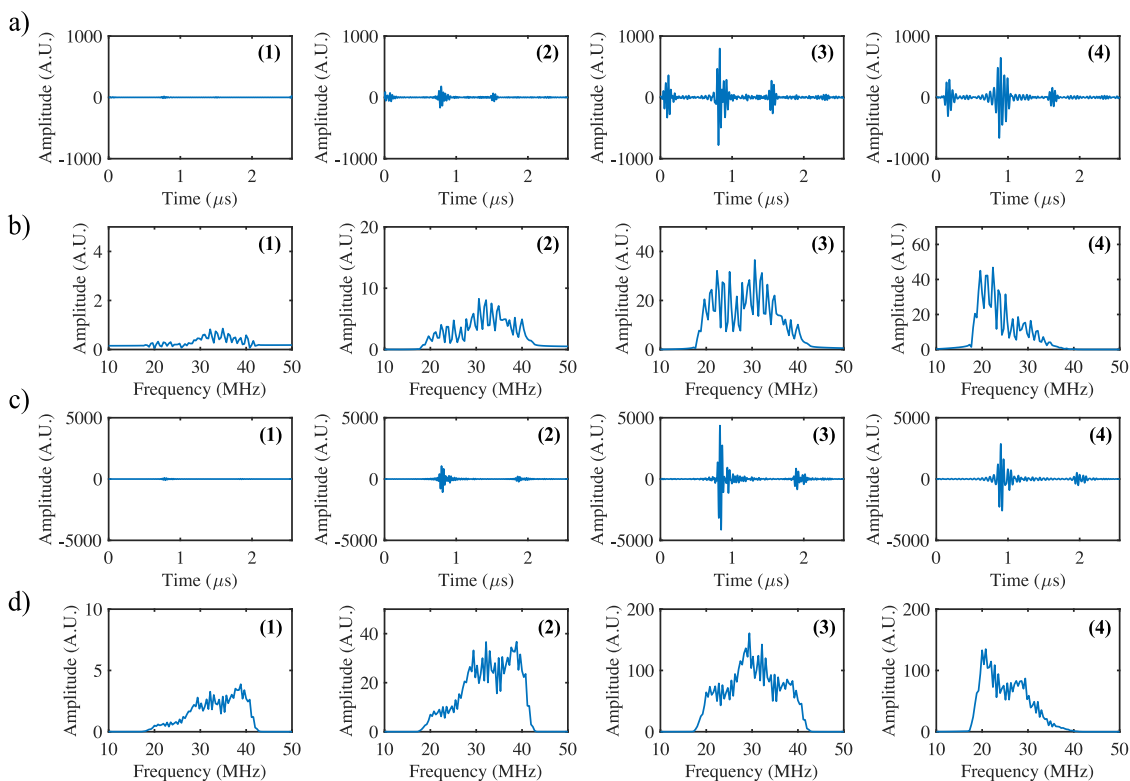
Fig. 11. It demonstrates the decomposition of the acoustic response signal into multiple decomposed time series after MODWT in both the time-domain (a), (c) as well as frequency domain (b), (d). Figures (a) and (b) highlight the characteristics of the response signals of fish scale at different decomposition levels and figures (c) and (d) highlight the characteristics of the response signal of polyimide (PI) at various decomposition levels. The time series shown in (1), (2), (3), and (4) are reconstructions using specific decomposition levels of wavelet coefficients.
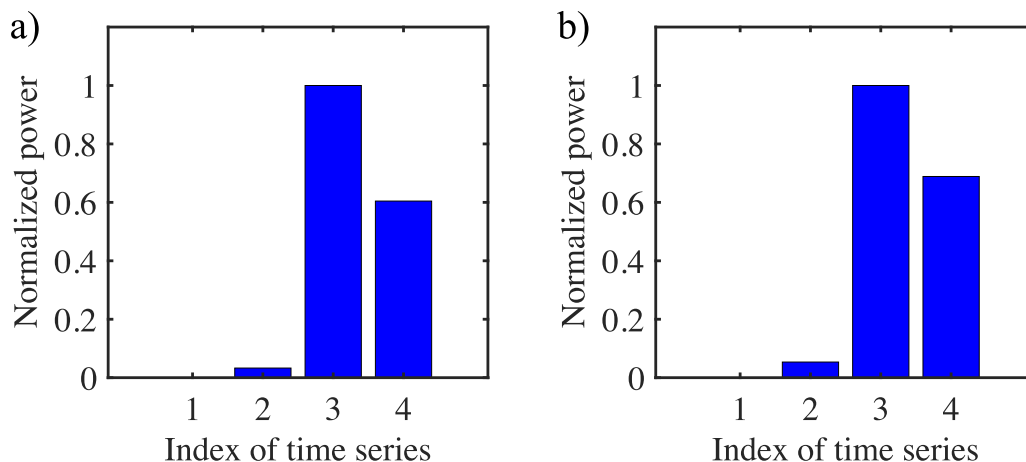

Fig. 12. The figures represent the normalized power of decomposed time series with respect to each other for (a) salmon and (b) polyimide (PI) samples, providing the basis for the selection of dominant time series.
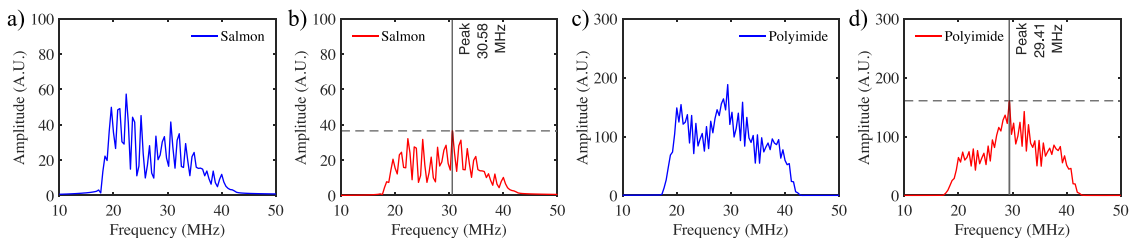

Fig. 13. Displayed in the figures are the frequency spectra of the true responses (a) fish scale or scale and (c) polyimide (PI), as well as the wavelet-transformed signals (b) and (d). These representations demonstrate the identification of primary frequencies which is a fundamental step in specific acoustic impedance calculation.
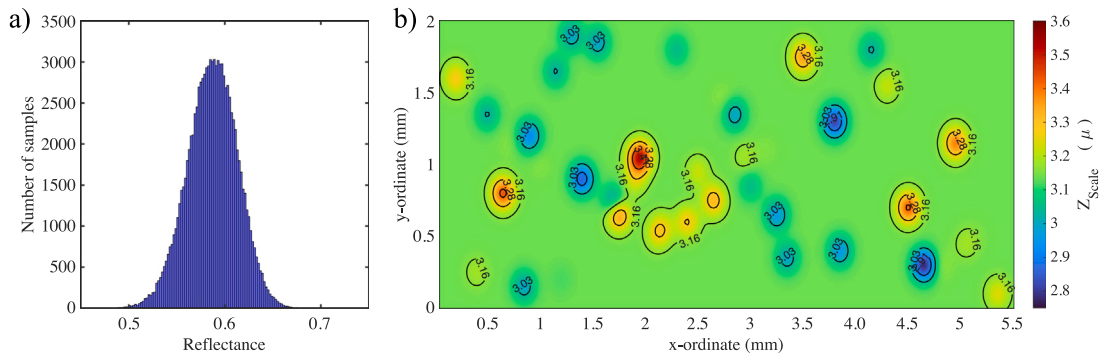
Fig. 14. Figure (a) presents the uncertainty considered in the reflectance and Figure (b) illustrates the distribution of estimated mean specific acoustic impedance values, providing a comprehensive view of how specific acoustic impedance varies across the entire domain of interest.
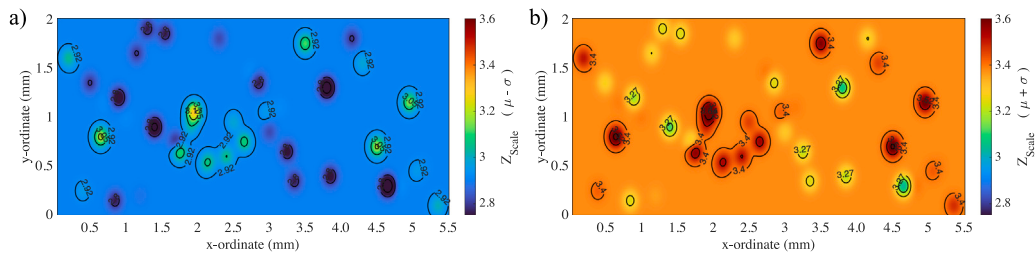

Fig. 15. Figure (a) presents the $\mu - \sigma$ values of the estimated stochastic specific acoustic impedance maps and Figure (b) illustrates the $\mu + \sigma$ values of the estimated stochastic specific acoustic impedance maps providing a comprehensive view of how specific acoustic impedance varies across the entire domain of interest with uncertain reflectance.

Table 2

It represents the corresponding frequency, measured and true specific acoustic impedance of fish scale along with their confidence bounds.

X (mm)	2.85	1.7	1.55	1.2	1.15	2.3	3.35	1.3	3	4.15
Y (mm)	1.35	0.75	1.85	0.2	1.65	1.8	0.35	1.9	0.85	1.8
Z_{sub}	12.8	12.8	12.8	12.8	12.8	12.8	12.8	12.8	12.8	12.8
S_{fish}	31.765	30.980	31.373	29.804	31.765	30.588	31.765	31.765	30.588	31.373
$S_{polyimide(PI)}$	29.412	29.020	29.020	29.020	29.804	29.020	29.412	29.412	29.020	29.412
S_{ratio}	1.080	1.068	1.081	1.027	1.066	1.054	1.080	1.080	1.054	1.067
μ_{Rpp}	0.595	0.595	0.595	0.595	0.595	0.595	0.595	0.595	0.595	0.595
σ_{Rpp}	0.024	0.024	0.024	0.024	0.024	0.024	0.024	0.024	0.024	0.024
μ_Z	2.785	2.856	2.779	3.090	2.866	2.933	2.785	2.785	2.933	2.861
$\mu_Z - \sigma_Z$	2.543	2.614	2.537	2.851	2.624	2.692	2.543	2.543	2.692	2.619
$\mu_Z + \sigma_Z$	3.035	3.105	3.029	3.337	3.115	3.181	3.035	3.035	3.181	3.110

uncertain reflectance enabled the development of a stochastic specific acoustic impedance map for fish scales. This map not only provides an average impedance value of 3.1 MRayl in this study but also visualizes the potential deviations due to uncertainties. Additionally, maximal overlap discrete wavelet transform and Kriging techniques enhanced the robustness of the impedance map, particularly for scenarios with limited data. Overall, this work offers a significant advancement for studying fish scale biomechanics. The proposed methods herein can be used to study the fish scale regeneration process, as scale loss during delousing strategies and fish skin lesions is of a serious concern in Norwegian aquaculture.

CRediT authorship contribution statement

Komal Agarwal: Writing – review & editing, Writing – original draft, Data curation. **Shivam Ojha:** Writing – review & editing, Writing – original draft, Software, Methodology, Formal analysis. **Roy Ambli Dalmo:** Writing – review & editing, Supervision, Funding acquisition. **Tore Seternes:** Writing – review & editing, Supervision, Resources. **Amit Shelke:** Writing – review & editing, Writing – original draft, Supervision, Resources, Investigation, Conceptualization. **Frank Melandsø:** Writing – review & editing, Visualization, Resources. **Anowarul Habib:** Writing – review & editing, Writing – original

draft, Supervision, Methodology, Funding acquisition, Data curation, Conceptualization.

Declaration of competing interest

The authors declare the following financial interests/personal relationships which may be considered as potential competing interests: UiT The Arctic University of Norway reports a relationship with Research Council of Norway that includes: funding grants. If there are other authors, they declare that they have no known competing financial interests or personal relationships that could have appeared to influence the work reported in this paper.

Data availability

The data sets used and/or analyzed during the current study are available from the corresponding author upon reasonable request.

Acknowledgment

References

[1] A. Briggs, O. Kolosov, Acoustic Microscopy, vol. 67, Oxford University Press, 2010.

[2] A. Habib, A. Shelke, M. Vogel, U. Pietsch, X. Jiang, T. Kundu, Mechanical characterization of sintered piezo-electric ceramic material using scanning acoustic microscope, Ultrasonics 52 (8) (2012) 989–995.

[3] M. Hofmann, R. Pflanzer, A. Habib, A. Shelke, J. Bereiter-Hahn, A. Bernd, R. Kaufmann, R. Sader, S. Kippenberger, Scanning acoustic microscopy—A novel noninvasive method to determine tumor interstitial fluid pressure in a xenograft tumor model, Transl. Oncol. 9 (3) (2016) 179–183.

[4] S. Brand, P. Czurratis, P. Hoffrogge, D. Temple, D. Malta, J. Reed, M. Petzold, Extending acoustic microscopy for comprehensive failure analysis applications, J. Mater. Sci., Mater. Electron. 22 (2011) 1580–1593.

[5] H. Yu, Scanning acoustic microscopy for material evaluation, Appl. Microsc. 50 (1) (2020) 1–11.

[6] S. Wagle, A. Habib, F. Melandsø, Ultrasonic measurements of surface defects on flexible circuits using high-frequency focused polymer transducers, Japan. J. Appl. Phys. 56 (7S1) (2017) 07JC05.

[7] E.S. Morokov, V.A. Demina, N.G. Sedush, K.T. Kalinin, E.A. Khramtsova, P.V. Dmitryakov, A.V. Bakirov, T.E. Grigoriev, V.M. Levin, S.N. Chvalun, Noninvasive high-frequency acoustic microscopy for 3D visualization of microstructure and estimation of elastic properties during hydrolytic degradation of lactide and ε-caprolactone polymers, Acta Biomater. 109 (2020) 61–72.

[8] D.M. King, C.M. Moran, J.D. McNamara, A.J. Fagan, J.E. Browne, Development of a vessel-mimicking material for use in anatomically realistic Doppler flow phantoms, Ultrasound Med. Biol. 37 (5) (2011) 813–826.

[9] B. Altun, I. Demirkan, E.O. Isik, O. Kocaturk, M.B. Unlu, B. Garipcan, Acoustic impedance measurement of tissue mimicking materials by using scanning acoustic microscopy, Ultrasonics 110 (2021) 106274.

[10] H. Okawai, K. Kobayashi, S. Nitta, An approach to acoustic properties of biological tissues using acoustic micrographs of attenuation constant and sound speed, J. Ultrasound Med.: Off. J. Am. Inst. Ultrasound Med. 20 (8) (2001) 891–907.

[11] Y. Saijo, M. Tanaka, H. Okawai, H. Sasaki, S.-I. Nitta, F. Dunn, Ultrasonic tissue characterization of infarcted myocardium by scanning acoustic microscopy, Ultrasound Med. Biol. 23 (1) (1997) 77–85.

[12] N. Hozumi, R. Yamashita, C.-K. Lee, M. Nagao, K. Kobayashi, Y. Saijo, M. Tanaka, N. Tanaka, S. Ohtsuki, Ultrasonic sound speed microscope for biological tissue characterization driven by nanosecond pulse, Acoust. Sci. Technol. 24 (6) (2003) 386–390.

[13] N. Hozumi, R. Yamashita, C.-K. Lee, M. Nagao, K. Kobayashi, Y. Saijo, M. Tanaka, N. Tanaka, S. Ohtsuki, Time–frequency analysis for pulse driven ultrasonic microscopy for biological tissue characterization, Ultrasonics 42 (1–9) (2004) 717–722.

[14] K. Raum, Microelastic imaging of bone, IEEE Trans. Ultrason. Ferroelectr. Freq. Control 55 (7) (2008) 1417–1431.

[15] M. Regauer, P. Jürgens, U. Budenhofer, M. Hartstock, W. Böcker, D. Bürklein, W. Mutschler, R. Sader, M. Schieker, Quantitative scanning acoustic microscopy compared to microradiography for assessment of new bone formation, Bone 38 (4) (2006) 564–570.

[16] S. Peck, G. Briggs, The caries lesion under the scanning acoustic microscope, Adv. Dent. Res. 1 (1) (1987) 50–63.

[17] I. Demirkan, G. Yaprak, C. Ceylan, E. Algul, C.O. Tomruk, B. Bilen, M.B. Unlu, Acoustic diagnosis of elastic properties of human tooth by 320 MHz scanning acoustic microscopy after radiotherapy treatment for head and neck cancer, Radiat. Oncol. 15 (1) (2020) 1–10.

[18] R. Vabø, E. Moen, S. Smoliński, Å. Husebø, N.O. Handegard, K. Malde, Automatic interpretation of salmon scales using deep learning, Ecol. Inform. 63 (2021) 101322.

[19] W.E. Ricker, Computation and interpretation of biological statistics of fish populations, Fish. Res. Board Can. Bull. 191 (1975) 1–382.

[20] Ø. Aas, A. Klemetsen, S. Einum, J. Skurdal, Atlantic Salmon Ecology, John Wiley & Sons, 2010.

[21] J.R. Butler, A. Radford, G. Riddington, R. Laughton, Evaluating an ecosystem service provided by Atlantic salmon, sea trout and other fish species in the River Spey, Scotland: the economic impact of recreational rod fisheries, Fish. Res. 96 (2–3) (2009) 259–266.

[22] J. Otero, A.J. Jensen, J.H. L'Abée-Lund, N.C. Stenseth, G.O. Storvik, L.A. Vøllestad, Contemporary ocean warming and freshwater conditions are related to later sea age at maturity in Atlantic salmon spawning in norwegian rivers, Ecol. Evol. 2 (9) (2012) 2192–2203.

[23] J. Erkinaro, Y. Czorlich, P. Orell, J. Kuusela, M. Falkegård, M. Länsman, H. Pulkkinen, C.R. Primmer, E. Niemelä, Life history variation across four decades in a diverse population complex of Atlantic salmon in a large subarctic river, Can. J. Fish. Aquat. Sci. 76 (1) (2019) 42–55.

[24] L. Hansen, T. Quinn, The marine phase of the Atlantic salmon (Salmo salar) life cycle, with comparisons to Pacific salmon, Can. J. Fish. Aquat. Sci. 55 (S1) (1998) 104–118.

[25] E. Niemelä, P. Orell, J. Erkinaro, J. Dempson, S. Brørs, M. Svenning, E. Hassinen, Previously spawned Atlantic salmon ascend a large subarctic river earlier than their maiden counterparts, J. Fish Biol. 69 (4) (2006) 1151–1163.

[26] K. Agarwal, R. Sahay, A. Baji, A.S. Budiman, Impact-resistant and tough helicoidally aligned ribbon reinforced composites with tunable mechanical properties via integrated additive manufacturing methodologies, ACS Appl. Polym. Mater. 2 (8) (2020) 3491–3504.

[27] K. Agarwal, R. Sahay, A. Baji, A.S. Budiman, Biomimetic tough helicoidally structured material through novel electrospinning based additive manufacturing, MRS Adv. 4 (43) (2019) 2345–2354.

[28] B. Ghosh, K. Agarwal, Viewing life without labels under optical microscopes, Commun. Biol. 6 (1) (2023) 559.

[29] B. Ghosh, J. Chatterjee, Advances in medical imaging for wound repair and regenerative medicine, in: Regenerative Medicine: Emerging Techniques to Translation Approaches, Springer, 2023, pp. 57–76.

[30] H. Song, Y. Yang, Uncertainty quantification in super-resolution guided wave array imaging using a variational Bayesian deep learning approach, NDT E Int. 133 (2023) 102753.

[31] M. Dohopolski, L. Chen, D. Sher, J. Wang, Predicting lymph node metastasis in patients with oropharyngeal cancer by using a convolutional neural network with associated epistemic and aleatoric uncertainty, Phys. Med. Biol. 65 (22) (2020) 225002.

[32] M.-H. Laves, S. Ihler, J.F. Fast, L.A. Kahrs, T. Ortmaier, Recalibration of aleatoric and epistemic regression uncertainty in medical imaging, 2021, arXiv preprint arXiv:2104.12376.

[33] N. Hiremath, V. Kumar, N. Motahari, D. Shukla, An overview of acoustic impedance measurement techniques and future prospects, Metrology 1 (1) (2021) 17–38.

[34] K. Kobayashi, S. Yoshida, Y. Saijo, N. Hozumi, Acoustic impedance microscopy for biological tissue characterization, Ultrasonics 54 (7) (2014) 1922–1928.

[35] N. Hozumi, S. Yoshida, K. Kobayashi, Three-dimensional acoustic impedance mapping of cultured biological cells, Ultrasonics 99 (2019) 105966.

[36] S.K. Mitra, Digital Signal Processing: a Computer-Based Approach, McGraw-Hill Higher Education, 2001.

[37] E.B. Prastika, T. Shintani, T. Kawashima, Y. Murakami, N. Hozumi, T.T.K. Soon, S. Yoshida, R. Nagaoka, K. Kobayashi, Time and frequency domain deconvolution for cross-sectional cultured cell observation using an acoustic impedance microscope, Ultrasonics 119 (2022) 106601.

[38] C.R. Cornish, C.S. Bretherton, D.B. Percival, Maximal overlap wavelet statistical analysis with application to atmospheric turbulence, Bound.-Layer Meteorol. 119 (2006) 339–374.

[39] G.P. Nason, Wavelet Methods in Statistics with R, Springer, 2008.

[40] D.B. Percival, A.T. Walden, Wavelet methods for time series analysis, vol. 4, Cambridge University Press, 2000.

[41] C.E. Rasmussen, C.K. Williams, et al., Gaussian processes for machine learning, vol. 1, Springer, 2006.

[42] T.T. Wong, R. Zhang, C. Zhang, H.-C. Hsu, K.I. Maslov, L. Wang, J. Shi, R. Chen, K.K. Shung, Q. Zhou, et al., Label-free automated three-dimensional imaging of whole organs by microtomy-assisted photoacoustic microscopy, Nat. Commun. 8 (1) (2017) 1386.

[43] E. Dong, Z. Song, Y. Zhang, S. Ghaffari Mosanenzadeh, Q. He, X. Zhao, N.X. Fang, Bioinspired metagel with broadband tunable impedance matching, Sci. Adv. 6 (44) (2020) eabb3641.

[44] P. Kumar, N. Yadav, M. Shamsuzzaman, K. Agarwal, F. Melandsø, A. Habib, Numerical method for tilt compensation in scanning acoustic microscopy, Measurement 187 (2022) 110306.

[45] S.K. Gupta, R. Pal, A. Ahmad, F. Melandsø, A. Habib, Image denoising in acoustic microscopy using block-matching and 4D filter, Sci. Rep. 13 (1) (2023) 13212.

[46] A. Habib, F. Melands, Chirp coded ultrasonic pulses used for scanning acoustic microscopy, in: 2017 IEEE International Ultrasonics Symposium, IUS, IEEE, 2017, pp. 1–4.

[47] Olympus, Polymer (PVDF) immersion transducers, 2010, https://www.olympus-ims.com/data/File/panametrics/panametrics-UT.en.pdf.

[48] T. Kundu, Mechanics of Elastic Waves and Ultrasonic Nondestructive Evaluation, CRC Press, 2019.

[49] J.D.N. Cheeke, Fundamentals and Applications of Ultrasonic Waves, CRC Press, 2017.

[50] S. Ojha, K. Agarwal, A. Shelke, A. Habib, Quantification of impedance and mechanical properties of Zeonor using scanning acoustic microscopy, Appl. Acoust. 221 (2024) 109981.

[51] N. Cressie, The origins of kriging, Math. Geol. 22 (1990) 239–252.

[52] E. Schulz, M. Speekenbrink, A. Krause, A tutorial on Gaussian process regression: Modelling, exploring, and exploiting functions, J. Math. Psych. 85 (2018) 1–16.